Surface Potential Equation for Low Effective Mass Channel Common Double-Gate MOSFET

Ananda Sankar Chakraborty and Santanu Mahapatra, *Senior Member, IEEE*

***Abstract*— Formulation of accurate yet computationally efficient surface potential equation (SPE) is the fundamental step toward developing compact models for low effective mass channel quantum well MOSFETs. In this paper, we propose a new SPE for such devices considering multisubband electron occupancy and oxide thickness asymmetry. Unlike the previous attempts, here, we adopt purely physical modeling approaches (such as without mixing the solutions from finite and infinite potential wells or using any empirical model parameter), while preserving the mathematical complexity almost at the same level. Gate capacitances calculated from the proposed SPE are shown to be in good agreement with numerical device simulation for wide range of channel thickness, effective mass, oxide thickness asymmetry, and bias voltages.**

***Index Terms*— III–V, compact modeling, double gate MOSFET, germanium.**

I. Introduction

To CATER the ever-increasing demand for operating speed along with low power consumption in integrated circuits, the use of ultrathin body multigate MOSFET with low effective mass channel material (e.g, Ge and III–V compounds) has been in recent focus of the semiconductor engineers [1]–[7]. Development of efficient compact models for these new transistors is thus crucial for their successful implementation in integrated circuits. Due to low density of states (DOS), the carriers are degenerate and the quantum confinement effect in the low effective mass quantum well is much higher than that of the Si MOSFETs. Such devices thus demonstrate unique quantum capacitance effect [8] in their C–V characteristics, which needs to be modeled accurately. In a standard drift-diffusion formalism based top–down compact modeling flow for Si MOSFET [9], [10], the surface potential equation (SPE) is first formulated by solving the governing 1-D Poisson equation analytically with Boltzmann distribution (under gradual channel approximation) [11], [12]. The equations for inversion charge density, drain current, and other parameters are then developed as a function of the surface potential. The quantum confinement effect is treated as a correction on this semiclassical solution. However, the real challenge for developing SPE for low DOS channel MOSFET is to find analytical solution of the Schrodinger–Poisson coupled differential equation system under the Fermi–Dirac distribution. It is imperative that a direct analytical solution of such coupled differential equation is not possible for all bias condition and one needs to find an approximate yet accurate solution technique. In a seminal work, Mudanai *et al.* [13] proposed one such solution by considering two energy subbands and wave function penetration inside the gate oxide. However, such solution is based on incoherent assumptions (i.e., mixing solution from finite and infinite potential well) and usage of empirical model parameter (in the expression of effective oxide capacitance). It is also found that the consideration of only two energy subbands is not enough to model the gate capacitance accurately for relatively thicker ($\geq$9 nm) and heavier ($\geq$0.1) effective mass channel. In other efforts [14], [15], the actual quantum well is modeled as a superposition of triangular and rectangular potential well involving empirical model parameters. All these works are based on symmetric oxide thickness-based common double gate (CDG) MOSFETs, where the coupling between the Schrodinger and Poisson equations is not clearly explained.

In this paper, we meticulously engineer the coupled Schrodinger–Poisson equation system to develop a purely physical SPE for undoped body CDG MOSFET without involving any empirical parameter. The effect of wave function penetration in gate oxide is modeled more physically as we never use the energy eigenvalues of an infinite potential well. We also include the effect of gate-oxide asymmetry, which could be useful for process variation and uncertainties. In addition, we include the effect of third energy subband to account for thicker channel and larger effective mass. We show that all these advancements are achieved without sacrificing the computational efficiency of the SPE. Proposed model is shown to be in excellent agreement with professional numerical device simulator (TCAD) [16] for wide gate bias range (untill 1.5 V), channel thickness (untill 10 nm), effective mass variation (0.02 to 0.1), and oxide asymmetry (100%).

II. Modeling Methodology

The coupled Schrodinger and Poisson equations system for such devices could be expressed as

$$\frac{d^2\psi}{dx^2} - \frac{2m}{\hbar^2}(qV(x) - E)\psi = 0 \quad (1)$$

Manuscript received January 19, 2017; accepted January 27, 2017. Date of publication February 21, 2017; date of current version March 22, 2017. The review of this paper was arranged by Editor J. Mateos.

The authors are with the Nano-Scale Device Research Laboratory, Department of Electronic Systems Engineering, Indian Institute of Science, Bengaluru 560012, India (e-mail: aschak86@gmail.com; santanu@dese.iisc.ernet.in).

Color versions of one or more of the figures in this paper are available online at http://ieeexplore.ieee.org.

Digital Object Identifier 10.1109/TED.2017.2661798

0018-9383 © 2017 IEEE. Personal use is permitted, but republication/redistribution requires IEEE permission.
See http://www.ieee.org/publications_standards/publications/rights/index.html for more information.

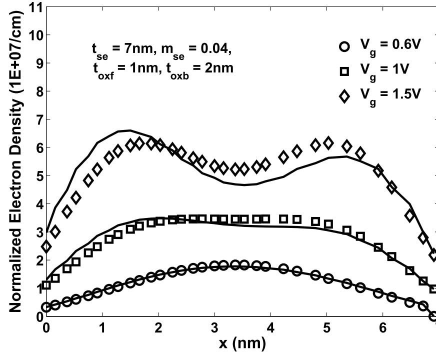

Fig. 1. Normalized electronic charge density $\rho(x)$ versus distance inside film. Both line $[\sum_{i=1}^{n_{\max}} f_i|\psi_i(x)|^2]$ and symbol $[\sum_{i=1}^{n_{\max}} f_i|\psi_i^{(0)}(x)|^2]$ are obtained from TCAD simulations.

$$\frac{dF}{dx} = -\frac{\rho(x)}{\epsilon} \tag{2}$$

where ψ is the electronic wave function, m = electron effective mass, q = elementary charge, $\hbar$ is the reduced Planck constant, ϵ is the material permittivity, $V(x)$ is the potential profile in the oxide-semiconductor system, E is the allowed subband energy, and F is the electric field. $\rho(x)$, the charge density, is given as [17]

$$\begin{aligned}\rho(x) &= q\frac{kTm}{\pi\hbar^2}\sum_{i=1}^{n_{\max}}|\psi_i(x)|^2\ln\left(1+e^{\frac{E_F-E_i}{kT}}\right)\\ &= q\frac{kTm}{\pi\hbar^2}\sum_{i=1}^{n_{\max}}|\psi_i(x)|^2 f_i\end{aligned} \tag{3}$$

where k is the Boltzmann constant, m = electron effective mass, E_F is the Fermi energy level, $E_i = i$th energy sub-band, T is the absolute temperature, $f_i = \ln(1+e^{(E_F-E_i)/kT})$, and $n_{\max}$ is the maximum number of energy subbands considered, which in this paper varies from 1 to 3. Integrating (2) with $\epsilon = \epsilon_{se}$ and $m = m_{se}$, we obtain

$$F(x) = F(x=x_0) - \frac{qkTm_{se}}{\pi\hbar^2\epsilon_{se}}\int_{x_0}^{x}\sum_{i=1}^{n_{\max}} f_i|\psi_i(x)|^2 dx \tag{4}$$

where x_0 is any point within the channel and $\epsilon_{se}(m_{se})$ = permittivity (electron effective mass) of semiconductor material. The Poisson equation in (4) gives the expression for electric field which on further integration yields the expression for electrostatic potential. Equations (1) and (4) are coupled through $\psi_i(x)$ and E_i (present in f_i and ψ_i) both of which are functions of electrostatic potential. In this paper, we obtain an approximate yet accurate analytical solution of this coupled differential equation systems by applying following two techniques.

1) $\psi_i(x) \simeq \psi_i^{(0)}(x)$, where $\psi_i^{(0)}(x)$ is the wave function for the ith subband at flat-band condition. Fig. 1 shows that $\sum_{i=1}^{n_{\max}} f_i|\psi_i(x)|^2$ and $\sum_{i=1}^{n_{\max}} f_i|\psi_i^{(0)}(x)|^2$ agree well even in higher bias condition as $\psi_i(x)$ is weak (sinusoidal) and f_i is a strong function of E_i.
2) E_i is expressed as an explicit function of electrostatic potential by applying perturbation on $E_i^{(0)}$ (energy eigenvalue at flat-band condition), without solving (1) at different bias conditions.

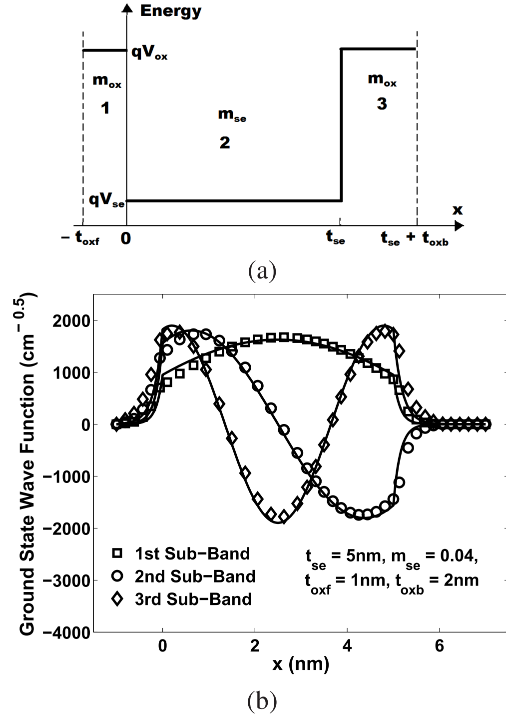

Fig. 2. (a) Schematic of the energy barrier profile in the direction perpendicular to the channel/gate–oxide interface (dashed lines indicating Dirichlet boundary condition) in a CDG MOSFET. (b) Wave function distribution at flat-band condition as obtained from model (line) and numerical device simulation (symbol).

Furthermore, to tackle the bias dependence of f_i, we represent (4) differently as

$$F(x) = F(x=x_0) - F_1\int_{x_0}^{x}\sum_{i=1}^{n_{\max}}\left|\psi_i^{(0)}(x)\right|^2 dx. \tag{5}$$

where F_1 is a quantity to be evaluated in the subsequent section IV. Clearly f_i varies with each subband energy level E_i, which is not the case for F_1. Rather in F_1, the cumulative effect of all subbands is expressed. We compensate this discrepancy by introducing correction factor in the energy perturbation model. Thus, the proposed solution finally leads to bulk/multigate MOSFET type SPE [11], [12], [18], [19], while implicitly maintaining the coupling between Schrodinger and Poisson equations even at high bias condition.

III. Subband Energy Calculation at Flat Band

The subband energies under flat-band condition for confinement are obtained through the solution of the Schrodinger equation with effective mass discontinuity across oxide–semiconductor interface.

The schematic of the energy barrier profile inside the device is given in Fig. 2(a), where region 2 denotes the semiconductor and regions 1 and 3 refer to the gate dielectric. The dashed lines at the ends of regions 1 and 3 indicate Dirichlet boundary condition or zero wave function penetration due to metal gate layers. Here, $V_{ox(se)}$ and m_{ox} are, respectively, the energy barrier height of oxide (semiconductor) and effective mass for oxide. $V_{ox(se)} = (E_{g,ox(se)}/2q)$, where $E_{g,ox(se)}$ is the bandgap

of oxide (semiconductor). The Schrodinger equations' for regions 1 and 3 are obtained from (1) by substituting $[m = m_{\rm ox}$ and $V(x) = V_{\rm ox} - V_{\rm se}]$ and for region 2 by substituting $[m = m_{\rm se}$ and $V(x) = 0]$. The flat-band electronic wave function $\psi^{(0)}(x)$ in regions 1–3 is

$$\psi^{(0)}(-t_{{\rm ox}f} \le x < 0) = C_2 e^{\alpha x} - C_1 e^{-\alpha x} \tag{6}$$

$$\psi^{(0)}(0 \le x \le t_{\rm se}) = A\cos(k_{\rm se}x) + B\sin(k_{\rm se}x) \tag{7}$$

$$\psi^{(0)}(t_{\rm se} < x \le t_{\rm se} + t_{{\rm ox}b}) = D_1 e^{-\alpha x} - D_2 e^{\alpha x} \tag{8}$$

where $\alpha = ((2m_{\rm ox}[q(V_{\rm ox} - V_{\rm se}) - E])^{1/2})/\hbar)$, $k_{\rm se} = (\sqrt{2m_{\rm se}E}/\hbar)$, and A, B, C_1, C_2, D_1, and D_2 are constants to be determined in subsequent steps.

Applying boundary conditions $\psi^{(0)}(-t_{{\rm ox}f}) = 0$, $\psi^{(0)}(t_{\rm se} + t_{{\rm ox}b}) = 0$, $\psi^{(0)}$ and $(1/m)(d\psi^{(0)}/dx)$ are continuous at semiconductor–oxide interfaces $x = 0$ and $x = t_{\rm se}$ along with the normalization of $\psi^{(0)}(x)$ over $x \in \{-t_{{\rm ox}f}, t_{\rm se} + t_{{\rm ox}b}\}$ we get the implicit energy solution for the flat-band condition and the constants as

$$\tan(k_{\rm se}t_{\rm se}) = r_0 \frac{\coth(\alpha t_{{\rm ox}f}) + \coth(\alpha t_{{\rm ox}b})}{1 - r_0^2 \coth(\alpha t_{{\rm ox}f})\coth(\alpha t_{{\rm ox}b})} \tag{9}$$

with

$$A = \frac{1}{\sqrt{\delta_1 + \delta_2 + \delta_3}}, \quad B = r_f A, \quad C_2 = \frac{A}{1 - e^{-2\alpha t_{{\rm ox}f}}}$$

$$C_1 = \frac{A e^{-2\alpha t_{{\rm ox}f}}}{1 - e^{-2\alpha t_{{\rm ox}f}}}, \quad D_1 = \frac{A e^{\alpha t_{\rm se}}}{1 - e^{-2\alpha t_{{\rm ox}b}}}$$

$$D_2 = \frac{A e^{-\alpha(t_{\rm se} + 2t_{{\rm ox}b})}}{1 - e^{-2\alpha t_{{\rm ox}b}}}, \quad \delta_1 = \frac{1 - e^{-4\alpha t_{{\rm ox}f}} - 4\alpha t_{{\rm ox}f} e^{-2\alpha t_{{\rm ox}f}}}{2\alpha(1 - e^{-2\alpha t_{{\rm ox}f}})^2}$$

$$r_0 = \frac{m_{\rm se}\alpha}{m_{\rm ox}k_{\rm se}}, \quad \delta_2 = \frac{1 + r_f^2}{2}\left(t_{\rm se} - \frac{\sin(2\beta) - sin(2\theta)}{2k_{\rm se}}\right)$$

$$r_f = r_0 \coth(\alpha t_{{\rm ox}f}), \quad \delta_3 = \frac{1 - e^{-4\alpha t_{{\rm ox}b}} - 4\alpha t_{{\rm ox}b} e^{-2\alpha t_{{\rm ox}b}}}{2\alpha(1 - e^{-2\alpha t_{{\rm ox}b}})^2}$$

$$\theta = \cot^{-1}(r_f), \quad \beta = k_{\rm se}t_{\rm se} + \theta.$$

By solving the implicit equation (9), we obtain the allowable energy subbands in flat-band condition and corresponding the wave functions from (6)–(8). Fig. 2(b) shows that the analytical solutions are in well agreement with numerical simulation result [16]. The complete solution of Schrodinger equations within the gate dielectric and channel enables us to develop SPE without mixing the solutions from finite and infinite potential well as done in previous work [13]. It is worth noting that (9) is independent of bias and thus its solution can be precalculated before run time to save the overall circuit simulation time [13].

IV. Complete Potential Profile Modeling

The schematic of the electric field distribution is given in Fig. 3. From (5) and Fig. 1, the electric fields that originate

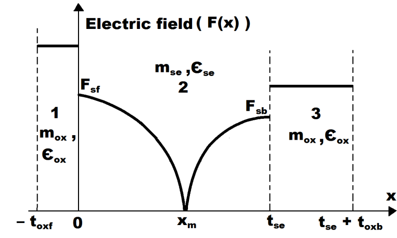

Fig. 3. Schematic of vertical electric field inside the channel.

from front and back semiconductor/dielectric interface take the following forms:

$$F(0 < x < x_m) = F_f(x) = F_{sf} - F_1 \int_0^x \sum_{i=1}^{n_{\rm max}} |\psi_i^{(0)}(x)|^2 dx \tag{10}$$

$$F(x_m < x < t_{\rm se}) = F_b(x) = F_{sb} - F_1 \int_x^{t_{\rm se}} \sum_{i=1}^{n_{\rm max}} |\psi_i^{(0)}(x)|^2 dx \tag{11}$$

where $F_{sf(b)} = (Q_{sf(b)}/\epsilon_{\rm se})$, $Q_{sf(b)}$ being front (back) surface charge per unit surface area $= C_{{\rm ox}f(b)}(V_g - \phi_{sf(b)})$, $C_{{\rm ox}f(b)} = \epsilon_{\rm ox}/t_{{\rm ox}f(b)} =$ front (back) oxide capacitance per unit area, and $\phi_{sf(b)}$ is front (back) surface potential. In Fig. 3, the point $x = x_m$ is the minimum potential point or zero electric field point inside the device. By evaluating (10) and (11) and making $F_f(x_m) = 0$ and $F_b(x_m) = 0$, we get $F_1 = \mu_f F_{sf} = \mu_b F_{sb}$, where

$$\mu_f = \frac{1}{\sum_{i=1}^{n_{\rm max}} \frac{A_i^2\left(1+r_{f,i}^2\right)}{2}\left[x_m - \frac{\sin(2\beta_{fm,i}) - \sin(2\theta_i)}{2k_{{\rm se},i}}\right]}$$

$$\mu_b = \frac{1}{\sum_{i=1}^{n_{\rm max}} \frac{A_i^2\left(1+r_{f,i}^2\right)}{2}\left[t_{\rm se} - x_m - \frac{\sin(2\beta_{{\rm bm},i}) - \sin(2\theta_i)}{2k_{{\rm se},i}}\right]}$$

$\beta_{fm,i} = k_{{\rm se},i}x_m + \theta_i$ and $\beta_{{\rm bm},i} = k_{{\rm se},i}(t_{\rm se} - x_m) + \theta_i$. Furthermore, we obtain $F_{sb} = \tau_0 F_{sf}$, where $\tau_0 = \mu_f/\mu_b$.

Integrating (10) and (11) within limits $x \in \{x_m, x\}$, we get the potential profile $\phi(x)$ inside the film as

$$\begin{aligned}\phi(0 < x < x_m) &= \phi_f(x) = \phi_m - F_{sf} \\ &\times \left[x - \mu_f \sum_{i=1}^{n_{\rm max}} \frac{A_i^2\left(1 + r_{f,i}^2\right)}{2}\left[\frac{cos(2k_{{\rm se},i}x + 2\theta_i)}{(2k_{{\rm se},i})^2}\right]\right] \\ &+ F_{sf}\left[\mu_f \sum_{i=1}^{n_{\rm max}} \frac{A_i^2\left(1 + r_{f,i}^2\right)}{2}\left[\frac{x^2}{2} + \frac{\sin(2\theta_i)}{2k_{{\rm se},i}}x\right] + y_{fm}\right]\end{aligned} \tag{12}$$

and

$$\phi(x_m < x < t_{\mathrm{se}}) = \phi_b(x) = \phi_m - F_{sb} \times \left[t_{\mathrm{se}} - x - \mu_b \sum_{i=1}^{n_{\max}} \frac{A_i^2(1+r_{f,i}^2)}{2} \times \left[\frac{\cos(2k_{\mathrm{se},i}x + 2\theta_i)}{(2k_{\mathrm{se},i})^2}\right] - y_{bm} \right] + F_{sb}\left[\mu_b \sum_{i=1}^{n_{\max}} \frac{A_i^2(1+r_{f,i}^2)}{2} \times \left[\frac{(t_{\mathrm{se}}-x)^2}{2} + \frac{\sin(2\theta_i)}{2k_{\mathrm{se},i}}(t_{\mathrm{se}}-x)\right]\right] \quad (13)$$

where ϕ_m = potential at $x = x_m$

$$y_{fm} = x_m - \mu_f \sum_{i=1}^{n_{\max}} \frac{A_i^2(1+r_{f,i}^2)}{2} \times \left[\frac{x_m^2}{2} + \frac{\sin(2\theta_i)}{2k_{\mathrm{se},i}}x_m + \frac{\cos(2\beta_{fm,i})}{(2k_{\mathrm{se},i})^2}\right]$$

$$y_{bm} = t_{\mathrm{se}} - x_m - \mu_b \sum_{i=1}^{n_{\max}} \frac{A_i^2(1+r_{f,i}^2)}{2} \times \left[\frac{(t_{\mathrm{se}}-x_m)^2}{2} + \frac{\sin(2\theta_i)}{2k_{\mathrm{se},i}}(t_{\mathrm{se}}-x_m) + \frac{\cos(2\beta_{fm,i})}{(2k_{\mathrm{se},i})^2}\right].$$

We also note that $\cos(2\beta_{fm,i}) = \cos(2\beta_{\mathrm{bm},i})$. We obtain front (back) surface potential $\phi_{sf(b)}$ by using $x = 0$ and $x = t_{\mathrm{se}}$, respectively, in (12) and (13) as

$$\phi_{sf(b)} = \phi_m + F_{sf(b)}\lambda_{f(b)m} \quad (14)$$

where, $\lambda_{f(b)m} = y_{f(b)m} - \mu_{f(b)} \sum_{i=1}^{n_{\max}}((A_i^2(1+r_{f,i}^2))/2)(\cos(2\theta_i)/(2k_{\mathrm{se},i})^2)$.

In (10)–(14), there are two unknowns x_m and ϕ_m. Therefore, we need to first calculate x_m in order to develop SPE that involves only one unknown: ϕ_m. We develop an approximate closed form expression of x_m by neglecting the effect of quantum confinement and assuming an uniform probability $\psi(0 \le x \le t_{\mathrm{se}}) = \zeta_0$ in the presence of electron everywhere inside the semiconductor. Thus, applying $\int_0^{t_{\mathrm{se}}}(\zeta_0)^2 dx = 1$ in (10) and (11) and solving further we get

$$x_m = t_{\mathrm{se}} \frac{1 + \frac{C_{\mathrm{oxb}}}{2C_{\mathrm{se}}}}{1 + \frac{C_{\mathrm{oxb}}}{C_{\mathrm{ox}f}} + \frac{C_{\mathrm{oxb}}}{C_{\mathrm{se}}}}. \quad (15)$$

So far, we have neglected the bias dependence of wave fuction $\psi(x)$ (Fig. 1) for the sake of simplicity, obtaining bias-independent closed form expression of x_m while in real scenario, it depends upon subband energy levels and hence on the applied bias. The approximated formulation of x_m is more accurate in weak inversion, because electrons are more uniformly dispersed across the film. From Fig. 4 we see that in strong inversion, (15) deviates from the self-consistent numerical simulation. However, such simplification yields accurate prediction of surface potential in all bias conditions as demonstrated in Section VII. This is due to the fact that in high bias condition, the electrons tend to move more toward the oxide–semiconductor interface, and hence the little deviation in x_m (~8%) prediction practically does not impose any significant effect on the surface potential solution.

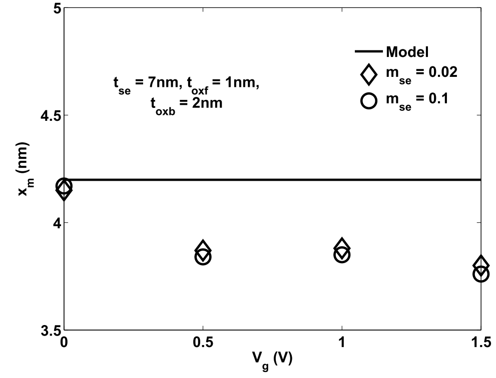

Fig. 4. Minimum potential point position x_m variation with effective gate voltage V_g for different effective masses. Line = model. Symbol = TCAD.

In this way, we develop the analytical models of electric field and potential considering the quantum-mechanical effect and without involving any empirical parameter.

V. Perturbation in Subband Energy Levels

To account for the energy shift due to enormous band bending because of high gate bias, a perturbation is applied over the flat-band condition energy obtained from (9). In this paper, a more generic and analytic form of the perturbation is provided unlike the previous paper [13], where the energy perturbation was modeled considering an infinite potential well.

It is quite evident from the solution of (9) that the gaps among successive subband levels increase gradually, for any given device thickness and effective mass. The third subband is much far from the Fermi level compared with the first and second ones, so in this paper, the charge contributions of the first and second subbands are modeled by the first-order perturbation only and the contribution of the third subband was modeled using both the first- and second-order perturbations.

Representing the first- and second-order perturbations for the ith subband as, E_i' and E_i'', respectively, their expressions are deduced as follows [20]:

$$E'_{f,i} = q\int_0^{x_m} \psi_i^{(0)}(x)[\phi_f(x) - \phi_{sf}]\psi_i^{(0)*}(x)dx \quad (16)$$

$$E'_{b,i} = q\int_{x_m}^{t_{\mathrm{se}}} \psi_i^{(0)}(x)[\phi_b(x) - \phi_{sb}]\psi_i^{(0)*}(x)dx \quad (17)$$

$$E''_{f,i} = \sum_{i \ne n} \frac{\left[q\int_0^{x_m} \psi_i^{(0)}(x)[\phi_f(x) - \phi_{sf}]\psi_n^{(0)*}(x)dx\right]^2}{E_i^{(0)} - E_n^{(0)}} \quad (18)$$

$$E''_{b,i} = \sum_{i \ne n} \frac{\left[q\int_{x_m}^{t_{\mathrm{se}}} \psi_i^{(0)}(x)[\phi_b(x) - \phi_{sb}]\psi_n^{(0)*}(x)dx\right]^2}{E_i^{(0)} - E_n^{(0)}}. \quad (19)$$

where $E'_{f(b),i}$ and $E''_{f(b),i}$ are, respectively, the first- and second-order energy perturbations due to front (back) gate potential profile. Integrations are bounded within the channel as we neglect the energy perturbation contributions from the front and back oxides due to the inherent fast decaying

exponential terms in the wave functions inside the oxides. The energy perturbations have the implicit discrepancy as we replace $\sum_{i=1}^{n_{\max}} f_i$ by F_1 in (5). To mitigate the model inaccuracy because of this discrepancy, two correction factors corresponding to front (back) gate $\gamma_{f(b)}$ (as discussed in Section II) are introduced in (16)–(19) as follows:

$$E'_{f(b),i} = -\gamma_{f(b)} \frac{qC^e_{\mathrm{ox}f(b)}(V_g - \phi_m)}{\epsilon_{\mathrm{se}}} A_i^2\left(1 + r_{f,i}^2\right) M'_{f(b),i} \tag{20}$$

$$E''_{f(b),i} = \left[\gamma_{f(b)} \frac{qC^e_{\mathrm{ox}f(b)}(V_g - \phi_m)}{\epsilon_{\mathrm{se}}}\right]^2 M''_{f(b),i} \tag{21}$$

where $M'_{f(b),i}$ and $M''_{f(b),i}$ are obtained by solving the integrations in (16) to (19) (see Appendix B for expressions), $\gamma_f = x_m/t_{\mathrm{se}}$, and $\gamma_b = (t_{\mathrm{se}} - x_m)/t_{\mathrm{se}}$ (derived in Appendix C).

Thus, the total first- and second-order energy perturbations E'_i and E''_i are given as

$$E'_i = E'_{f,i} + E'_{b,i} = -M'_i(V_g - \phi_m) \tag{22}$$

$$E''_i = E''_{f,i} + E''_{b,i} = M''_i(V_g - \phi_m)^2 \tag{23}$$

with

$$M'_i = \frac{qA_i^2\left(1 + r_{f,i}^2\right)}{\epsilon_{\mathrm{se}}}\left[\gamma_f C^e_{\mathrm{ox}f} M'_{f,i} + \gamma_b C^e_{\mathrm{oxb}} M'_{b,i}\right] \tag{24}$$

$$M''_i = \left(\frac{q}{\epsilon_{\mathrm{se}}}\right)^2 \left[\left(\gamma_f C^e_{\mathrm{ox}f}\right)^2 M''_{f,i} + \left(\gamma_b C^e_{\mathrm{oxb}}\right)^2 M''_{b,i}\right]. \tag{25}$$

Equations (24) and (25) represent the final forms of first- and second-order energy perturbations, which are purely physically developed. The coefficients M'_i and M''_i are functions of material and device geometry parameters and hence can be computed at setup time of circuit simulation.

VI. Formulation of Surface Potential

In any MOS structure, neglecting any interfacial trapped charges, the total gate charge per unit surface area (Q_g) should balance the charge per unit surface area inside semiconductor (Q_{se}). Again Q_g has two components Q_{gf} and Q_{gb} due to front and back gates, respectively. As the charges at the two interfaces are due to respective gates [13], we may assume that individual components of gate charges constitute the charge at corresponding oxide–semiconductor interfaces, or $Q_{gf} = Q_{sf}$ and $Q_{gb} = Q_{sb}$. Hence, $Q_g = Q_{sf} + Q_{sb}$.

To account for the charge centroid effect [13], we define two equivalent oxide capacitances $C^e_{\mathrm{ox}f}$ and C^e_{oxb} such that $Q_{sf(b)} = C_{\mathrm{ox}f(b)}(V_g - \phi_{sf(b)}) = C^e_{\mathrm{ox}f(b)}(V_g - \phi_m)$. Using the linear relationship between $\phi_{sf(b)}$ and ϕ_m in (14), we obtain

$$Q_{sf(b)} = C_{\mathrm{ox}f(b)}(V_g - \phi_m - F_{sf(b)}\lambda_{f(b)m}). \tag{26}$$

Using $F_{sf(b)} = (Q_{sf(b)}/\epsilon_{\mathrm{se}})$ and rearranging (26), we obtain the generalized expression for $C^e_{\mathrm{ox}f(b)}$

$$C^e_{\mathrm{ox}f(b)} = \frac{Q_{sf(b)}}{V_g - \phi_m} = \frac{C_{\mathrm{ox}f(b)}}{1 + \frac{\lambda_{f(b)m}}{\epsilon_{\mathrm{se}}} C_{\mathrm{ox}f(b)}}. \tag{27}$$

By using boundary condition $F(x = 0) = F_{sf}$, $F(x = x_m) = 0$ and $F(x = t_{\mathrm{se}}) = F_{sb}$ in (4) and combining the results, we get

$$\epsilon_{\mathrm{se}}(F_{sf} + F_{sb}) = \frac{qkTm_{\mathrm{se}}}{\pi\hbar^2} \sum_{i=1}^{n_{\max}} f_i \int_0^{t_{\mathrm{se}}} |\psi_i(x)|^2 dx. \tag{28}$$

It is interesting to note that Left Hand Side of (28) is the total charge per unit area Q_{se}. In the Right Hand Side, we may reasonably put $\int_0^{t_{\mathrm{se}}} |\psi_i(x)|^2 dx \approx 1$ neglecting the leakage into the front and back oxides due to the innate fast dropping exponential terms in $\psi_i(-t_{\mathrm{ox}f} \le x < 0)$ and $\psi_i(t_{\mathrm{se}} < x \le t_{\mathrm{se}} + t_{\mathrm{ox}b})$ [(6) and (8), respectively]. Hence

$$Q_{\mathrm{se}} \approx \frac{qkTm_{\mathrm{se}}}{\pi\hbar^2} \sum_{i=1}^{n_{\max}} f_i. \tag{29}$$

Equation (29) follows exactly the expression of total charge per unit surface area in an undoped semiconductor considering Two-Dimensional Electron Gas system, degeneracy factor = 1 [13], and Fermi–Dirac statistics [21]. This may be elaborated as

$$Q_{\mathrm{se}} = C_{\mathrm{QMe}} U_t \sum_{i=1}^{n_{\max}} \ln\left(1 + e^{\left[\frac{q\phi_m - \left(E_i^{(0)} + E'_i - E''_i\right) - \frac{E_{g,(se)}}{2} - qV_{ch}}{kT}\right]}\right) \tag{30}$$

where $C_{\mathrm{QMe}} = (q^2 m_{\mathrm{se}}/\pi\hbar^2)$, V_{ch} = channel potential, $E_i^{(0)}$ obtained from (9), and $U_t = kT/q$ = thermal voltage. Replacing E'_i and E''_i from (22) and (23) into (30) and using $\delta = \exp(-((E_{g,se} + 2qV_{ch})/2kT))$, we obtain

$$Q_{\mathrm{se}} = C_{\mathrm{QMe}} U_t \sum_{i=1}^{n_{\max}} \ln\left(1 + \delta e^{\left[\frac{q\phi_m - \left[E_i^{(0)} - M'_i(V_g - \phi_m) - M''_i(V_g - \phi_m)^2\right]}{kT}\right]}\right). \tag{31}$$

As discussed earlier, the third subband is furthest from the Fermi level hence its interactions with the first and second subbands are to be modeled more precisely. Hence, besides applying first- and second-order perturbations to capture the charge contribution of third subband for a wide range of device thickness (5–10 nm) and effective masses (0.02–0.1), C_{QMe} associated with the third subband is further modeled as a resultant capacitance (C^r_{QMe}) as developed in Appendix A.

Noting $Q_{\mathrm{se}} = Q_{sf} + Q_{sb}$ from previous steps and from (27) and (31), we finally formulate the SPE as

$$\left(C^e_{\mathrm{ox}f} + C^e_{\mathrm{oxb}}\right)(V_g - \phi_m) = U_t \sum_{i=1}^{n_{\max}} C_{qi} \times \ln\left(1 + \delta e^{\left[\frac{q\phi_m - \left[E_i^{(0)} - M'_i(V_g - \phi_m) - M''_i(V_g - \phi_m)^2\right]}{kT}\right]}\right). \tag{32}$$

For $i \in \{1, 2\}$, $C_{qi} = C_{\mathrm{QMe}}$ and $M''_i = 0$ and for $i = 3$, $C_{qi} = C^r_{\mathrm{QMe},3}$ obtained from (A-4). Once ϕ_m is obtained from the numerical solution of (32), $\phi_{sf(b)}$ can be found out from (14).

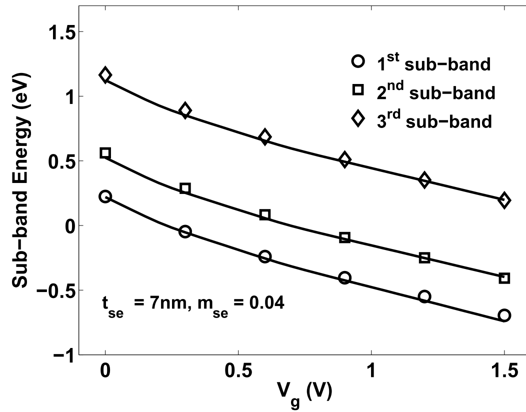

Fig. 5. Subband energy variation with effective gate voltage V_g. Line = model. Symbol = TCAD.

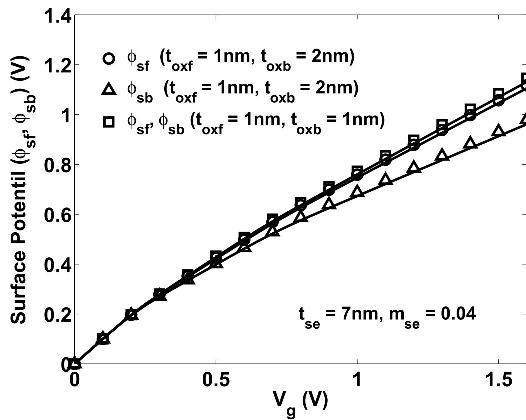

Fig. 6. Front and back surface potential variations with effective gate voltage V_g for various asymmetries in oxide thickness. Line = model. Symbol = TCAD.

VII. Results and Discussion

The proposed model has been validated against the ATLAS numerical device simulator, which is a part of Silvaco TCAD suite [16]. In ATLAS simulation environment, to solve the coupled Schrodinger–Poisson equations inside oxide and semiconductor, we use SCHRO and OX.SCHRO commands along with the QUANTUM model. The fixed material parameters used are: $V_{\text{ox}} = 3.9$ eV, $V_{\text{se}} = 0.133$ eV, $\epsilon_{\text{se}} = 13.6\epsilon_0$, and $\epsilon_{\text{ox}} = 3.9\epsilon_0$, where ϵ_0 is the permittivity of free space. All the effective masses are multiplied with m_0, the free electron mass. V_{ch} is set to 0.

The effect of bias voltage on the subband energy levels is shown in Fig. 5, which depicts that the energy perturbation model yields good agreement with TCAD simulation.

Fig. 6 demonstrates the surface potential versus effective gate voltage plot for both symmetric and asymmetric devices. It is worth noting that due to strong confinement and Fermi–Dirac distribution of carriers, unlike a Si MOSFET, the surface potential does not saturate with increasing gate voltage. Fig. 7 shows the potential profile inside the device and the validity of the proposed x_m model. The gate capacitance per unit width calculated from the surface potential solution is shown in Figs. 8 and 9. It can be seen that the proposed

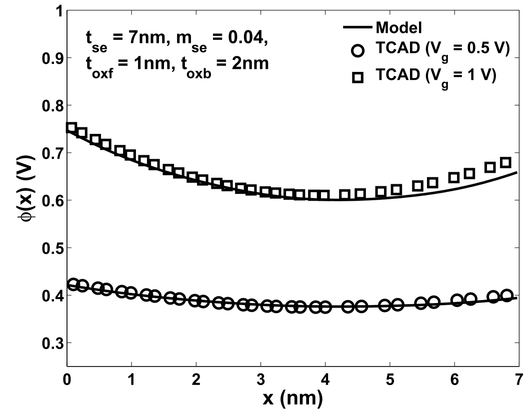

Fig. 7. Potential variation with distance inside semiconductor. Line = model. Symbol = TCAD.

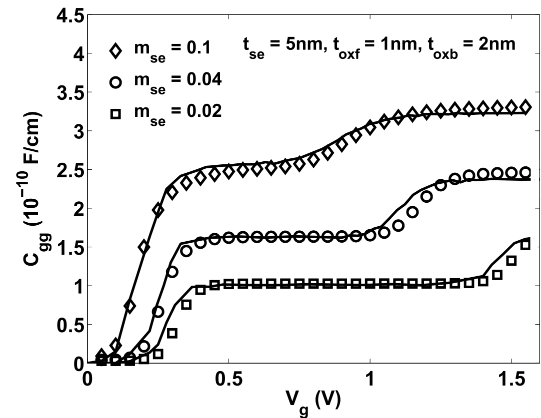

Fig. 8. Total gate capacitance per unit width C_{gg} versus effective gate voltage V_g for 5-nm-thick device with 100% asymmetry in front and back oxide thicknesses. $n_{\text{max}} = 2$. Line = model. Symbol = TCAD.

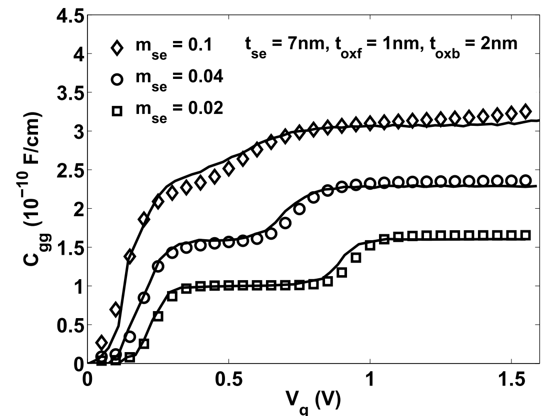

Fig. 9. Total gate capacitance per unit width C_{gg} versus effective gate voltage V_g for 7-nm-thick device with 100% asymmetry in front and back oxide thicknesses. $n_{\text{max}} = 2$. Line = model. Symbol = TCAD.

model accurately predicts the quantized nature of the gate capacitance, which is expected in such low effective mass channel ultrathin body devices. The importance of the third energy subband is demonstrated in Fig. 10. The previous model [13] fails to predict the capacitance accurately even within $V_g < 1$ V range for the relatively thicker body ($\geq$9 nm) and higher effective mass ($\geq$0.1) devices.

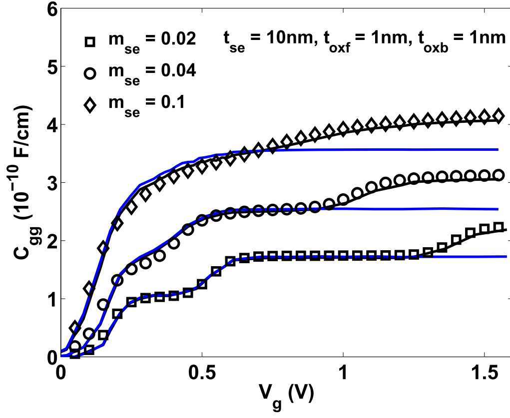

Fig. 10. Comparison of gate capacitance per unit width C_{gg} model. Black line = proposed model with $n_{\max} = 3$. Blue line = [13]. Symbol = TCAD.

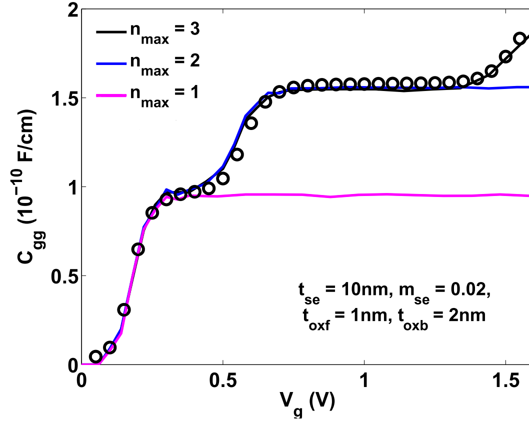

Fig. 11. Total gate capacitance per unit width C_{gg} versus effective gate voltage V_g for varying maximum number of subbands $n_{\max}$. Line = model. Symbol = TCAD.

Another salient feature of the proposed SPE (32) is that it could be solved for $n_{\max} = 1$, 2 or 3, as shown in Fig. 11. The subbands get activated gradually as gate bias increases. This gives the user the flexibility to choose $n_{\max}$ as per design requirement and thus to save the simulation time. We further note that additional mathematical complexity due to the inclusion of oxide thickness asymmetry is consumed in energy eigenvalue (9), which is independent of bias condition and thus could be computed during the setup time of circuit simulation. The complexity of (32) is the same as that of previous work [13] for $n_{\max} = 2$. Inclusion of the third subband just add one extra exponential and logarithmic term in (32).

VIII. Conclusion

We present a computationally efficient SPE for low effective mass channel ultrathin body CDG MOSFET. Several physical effects, e.g., wave function penetration in gate oxide, multi-subband electron occupancy, oxide thickness asymmetry, and so on are considered while developing the model. Proposed model is free from any empirical model parameters and found to be in good agreement with numerical device simulation for wide range of device and material parameters.

Appendix A

The inversion charge per unit area contribution due to the third subband is given as

$$Q_{\mathrm{se},3} = C_{\mathrm{QMe}} U_t \ln\left(1 + \delta e^{\left[\frac{q\phi_s - \left(E_3^{(0)} + E_3' - E_3''\right)}{kT}\right]}\right) \quad \text{(A-1)}$$

where ϕ_s is the average surface potential in the semiconductor and given as $(x_m/t_{\mathrm{se}})\phi_{sf} + ((t_{\mathrm{se}} - x_m)/t_{\mathrm{se}})\phi_{sb}$. In high gate bias condition, the term $q\phi_s$ in (A-1) becomes large enough to make the exponential term dominant, which leads to

$$Q_{\mathrm{se},3} \approx C_{\mathrm{QMe}}\left(\phi_s - \frac{E_3^{(0)} + E_3'}{q} - \frac{E_{g,se}}{2q} - V_{ch}\right). \quad \text{(A-2)}$$

In (A-2), we neglect the second-order perturbation term E_3'' to keep the model simple. As the effect of second-order perturbation is already inculcated in the main SPE (32), it will be redundant to use the same in the expression of resultant C_{QMe}. Using (14) and (22), we finally arrive at

$$Q_{\mathrm{se},3} = C_{\mathrm{QMe},3}^r\left(\phi_m - \frac{E_3^{(0)}}{q} - \frac{E_{g,se}}{2q} - V_{ch}\right) \quad \text{(A-3)}$$

where $C_{\mathrm{QMe},3}^r$ is the resultant C_{QMe} for the third subband and is given by

$$C_{\mathrm{QMe},3}^r = \frac{C_{\mathrm{QMe},3}}{1 + \frac{C_{\mathrm{QMe}}}{1+\tau_0}\left(\frac{G_3' - \lambda_A}{\epsilon_{\mathrm{se}}}\right)} \quad \text{(A-4)}$$

with $G_3' = (x_m/t_{\mathrm{se}})M_{f,3}' + ((t_{\mathrm{se}} - x_m)/t_{\mathrm{se}})\tau_0 M_{b,3}'$ and $\lambda_A = (x_m/t_{\mathrm{se}})\lambda_{fm} + ((t_{\mathrm{se}} - x_m)/t_{\mathrm{se}})\tau_0\lambda_{bm}$.

Appendix B

$$\begin{aligned}
&M_{f(b),i}' \\
&= (\lambda_{f(b)m} - y_{f(b)m})\left[\frac{x_m}{2} - \frac{\sin(2\beta_{f(b)m,i}) - \sin(2\theta_i)}{4k_{\mathrm{se},i}}\right] \\
&\quad + \left[1 - \mu_{f(b)}\sum_{j=1}^{n_{\max}} \frac{A_j^2\left(1 + r_{f,j}^2\right)\sin(2\theta_j)}{4k_{\mathrm{se},j}}\right] \\
&\quad \times \left[\frac{x_m^2}{4} + \frac{x_m \sin(2\beta_{f(b)m,i})}{4k_{\mathrm{se},i}} + \frac{\cos(2\theta_i) - cos(2\beta_{f(b)m,i})}{8k_{\mathrm{se},i}^2}\right] \\
&\quad - \frac{\mu_{f(b)}}{8}\sum_{j=1}^{n_{\max}} A_j^2\left(1 + r_{f,j}^2\right) \\
&\quad \times \left[\frac{x_m^3}{3} - \frac{x_m^2 \sin(2\beta_{f(b)m,i})}{2k_{\mathrm{se},i}} - \frac{x_m \cos(2\beta_{f(b)m,i})}{2k_{\mathrm{se},i}^2}\right. \\
&\qquad \left. + \frac{\sin(2\beta_{f(b)m,i}) - sin(2\theta_i)}{4k_{\mathrm{se},i}^3}\right] \\
&\quad - \frac{\mu_{f(b)}}{4}\sum_{j=1}^{n_{\max}} l_j\left[\frac{\sin(\beta_{f(b)m,j}) - sin(\theta_j)}{2k_{\mathrm{se},j}}\right] \\
&\quad + \frac{\mu_{f(b)}}{4} l_i\left[x_m + \frac{\sin(4\beta_{f(b)m,i}) - \sin(4\theta_i)}{4k_{\mathrm{se},i}}\right] \\
&\quad + \frac{\mu_{f(b)}}{4}\sum_{j\neq i} l_j
\end{aligned}$$

$$S(R)_{1f(b),ij} = \frac{\sin(\beta_{f(b)m,i} - (+)\beta_{f(b)m,j}) - \sin(\theta_i - (+)\theta_j)}{k_{\mathrm{se},i} - (+)k_{\mathrm{se},j}} \tag{B-3}$$

$$\begin{aligned} S(R)_{2f(b),ij} = &[(k_{\mathrm{se},i} - (+)k_{\mathrm{se},j})x_m \sin(\beta_{f(b)m,i} - (+)\beta_{f(b)m,j}) \\ &+ \cos(\beta_{f(b)m,i} - (+)\beta_{f(b)m,j}) - \cos(\theta_i - (+)\theta_j)] \\ &\times \left[1 - \mu_{f(b)} \sum_{n=1}^{n_{\max}} \frac{A_n^2(1 + r_{f,n}^2)\sin(2\theta_n)}{4k_{\mathrm{se},n}}\right] / (k_{\mathrm{se},i} - (+)k_{\mathrm{se},j})^2 \end{aligned} \tag{B-4}$$

$$\begin{aligned} S(R)_{3f(b),ij} = &\left[(k_{\mathrm{se},i} - (+)k_{\mathrm{se},j})^2 x_m^2 \sin(\beta_{f(b)m,i} - (+)\beta_{f(b)m,j})\right. \\ &+ 2(k_{\mathrm{se},i} - (+)k_{\mathrm{se},j})x_m \cos(\beta_{f(b)m,i} - (+)\beta_{f(b)m,j}) \\ &\left.+ 2\sin(\theta_i - (+)\theta_j) - 2\sin(\beta_{f(b)m,i} - (+)\beta_{f(b)m,j})\right] \\ &\times \left[\frac{\mu_{f(b)}}{4(k_{\mathrm{se},i} - (+)k_{\mathrm{se},j})^3} \sum_{n=1}^{n_{\max}} A_n^2 (1 + r_{f,n}^2)\right] \end{aligned} \tag{B-5}$$

$$\begin{aligned} S(R)_{4f(b),ij} = &\sum_{n=1}^{n_{\max}} \frac{l_n}{2} \left[\frac{\sin(2\beta_{f(b)m,n} + \beta_{f(b)m,i} - (+)\beta_{f(b)m,j}) - sin(2\theta_n + \theta_i - (+)\theta_j)}{2k_{\mathrm{se},n} + k_{\mathrm{se},i} - (+)k_{\mathrm{se},j}}\right. \\ &\left.+ \frac{\sin(2\beta_{f(b)m,n} + \beta_{f(b)m,j} - (+)\beta_{f(b)m,i}) - sin(2\theta_n + \theta_j - (+)\theta_i)}{2k_{\mathrm{se},n} + k_{\mathrm{se},j} - (+)k_{\mathrm{se},i}}\right]. \end{aligned} \tag{B-6}$$

$$\begin{aligned} &\times \left[\frac{\sin[2(\beta_{f(b)m,j} + \beta_{f(b)m,i})] - sin[2(\theta_j + \theta_i)]}{2(k_{\mathrm{se},j} + k_{\mathrm{se},i})}\right] \\ &+ \frac{\mu_{f(b)}}{4} \sum_{j \neq i} l_j \\ &\times \left[\frac{\sin[2(\beta_{f(b)m,j} - \beta_{f(b)m,i})] - sin[2(\theta_j - \theta_i)]}{2(k_{\mathrm{se},j} - k_{\mathrm{se},i})}\right] \end{aligned} \tag{B-1}$$

and

$$\begin{aligned} M''_{f(b),i} = &\sum_{j \neq i} \frac{\left(\frac{A_i A_j}{2}\right)^2 (1 + r_{f,i}^2)(1 + r_{f,j}^2)}{E_i - E_j} \\ &\times [(S_{1f(b),ij} - R_{1f(b),ij}) + (S_{2f(b),ij} - R_{2f(b),ij}) \\ &- (S_{3f(b),ij} - R_{3f(b),ij}) - (S_{4f(b),ij} - R_{4f(b),ij})]^2. \end{aligned} \tag{B-2}$$

Here

$$l = \frac{A^2(1 + r_f^2)}{8k_{\mathrm{se}}^2}$$

with (B-3)–(B-6) shown at the top of this page.

Appendix C

The discrepancy arisen due to substitution of F_1 instead of $\sum_{i=1}^{n_{\max}} f_i$ [see (4) and (5)] has been compensated in energy perturbations [see (20) and (21)] by the introduction of correction factors $\gamma_{f(b)}$ corresponding to front (back) gate. Hence, from (4) and (5)

$$\frac{qkTm}{\pi\hbar^2\epsilon} \int_0^{x_m} \sum_{i=1}^{n_{\max}} f_i |\psi_i(x)|^2 dx \equiv \gamma_f F_1 \int_0^{x_m} \sum_{i=1}^{n_{\max}} \left|\psi_i^{(0)}(x)\right|^2 dx. \tag{C-1}$$

By applying the boundary condition [$F(x = 0) = F_{sf}$ and $F(x = x_m) = 0$] in (4)

$$\gamma_f = \frac{F_{sf}}{F_1 \int_0^{x_m} \sum_{i=1}^{n_{\max}} \left|\psi_i^{(0)}(x)\right|^2 dx}. \tag{C-2}$$

For the sake of simplicity, we aimed to model the correction factor γ_f as a factor-independent of subband energy and hence applied bias and all kinds of perturbation. Hence, without losing generality, we again assume an uniform probability $\psi^{(0)}(0 \le x \le t_{\mathrm{se}}) = \zeta_0$ in the presence of electron everywhere inside the semiconductor (Section IV). Thus, reapplying $\int_0^{t_{\mathrm{se}}} (\zeta_0)^2 dx = 1$ in (10) and putting boundary condition [$F(x = 0) = F_{sf}$ and $F(x = x_m) = 0$], we get

$$F_1 = F_{sf} \frac{t_{\mathrm{se}}}{x_m}. \tag{C-3}$$

Hence, applying (C-3) in (C-2), we get

$$\gamma_f = \frac{x_m}{t_{\mathrm{se}}} \frac{1}{\int_0^{x_m} \sum_{i=1}^{n_{\max}} \left|\psi_i^{(0)}(x)\right|^2 dx}. \tag{C-4}$$

From the results of numerical device simulations in TCAD over device thickness varying from 5 to 10 nm, applied bias varying from 0 to 1.5 V, and effective mass varying from 0.02 to 0.1, we have seen that mostly first two subbands are filled throughout the aforementioned parametric range. Besides, the numerical simulation infers $\int_0^{x_m} \sum_{i=1}^{2} |\psi_i^{(0)}(x)|^2 dx \approx 1$. It can be explained physically as the first two subbands are mostly filled hence $\int_0^{t_{\mathrm{se}}} |\psi_1^{(0)}(x)|^2 dx$ and $\int_0^{t_{\mathrm{se}}} |\psi_2^{(0)}(x)|^2 dx$ are individually $= 1$. So, the combined probability that the electron is within $0 \le x \le x_m$ for subband 1 or 2 can be ≈ 1. For higher bias, the combined probability nears more to 1. Hence, (C-4) takes the form

$$\gamma_f = x_m / t_{\mathrm{se}}. \tag{C-5}$$

By applying similar steps on (11) and using boundary condition [$F(x = t_{\mathrm{se}}) = F_{sb}$ and $F(x = x_m) = 0$], one shall arrive at

$$\gamma_b = (t_{\mathrm{se}} - x_m) / t_{\mathrm{se}}. \tag{C-6}$$

Thus, from (C-5) and (C-6), we obtain simple bias-independent expressions of correction factors γ_f and γ_b, respectively.

Acknowledgment

The authors would like to thank the anonymous reviewers for their constructive comments and suggestions.

References

[1] (2013). *International Technology Roadmap for Semiconductors (ITRS)*. [Online]. Available: http://www.itrs2.net
[2] J. A. del Alamo, "Nanometre-scale electronics with III–V compound semiconductors," *Nature*, vol. 479, pp. 317–323, Nov. 2011.
[3] Y. Sun *et al.*, "High-performance CMOS-compatible self-aligned $In_{0.53}Ga_{0.47}As$ MOSFETs with GMSAT over 2200 μS/μm at $V_{DD} = 0.5$ V," in *IEDM Tech. Dig.*, Dec. 2014, pp. 25.3.1–25.3.4.
[4] Y. Kamata, "High-k/Ge MOSFETs for future nanoelectronics," *Mater. Today*, vol. 11, nos. 1–2, pp. 30–38, Jan./Feb. 2008.
[5] S. Adachi, *Properties of Group-IV, III–V and II–VI Semiconductors*. Hoboken, NJ, USA: Wiley, 2005.
[6] C. Claeys and E. Simoen, *Germanium-Based Technologies From Materials to Devices*. New York, NY, USA: Elsevier, 2007.
[7] M. K. Hudait and R. Chau, "Integrating III–V on silicon for future nanoelectronics," in *Proc. IEEE Compound Semiconductor Integr. Circuits Symp. (CSIC)*, Oct. 2008, pp. 1–2.
[8] S. Luryi, "Quantum capacitance devices," *Appl. Phys. Lett.*, vol. 52, no. 6, pp. 501–503, 1988.
[9] Y. S. Chauhan *et al.*, *FinFET Modeling for IC Simulation and Design: Using the BSIM-CMG Standard*. San Diego, CA, USA: Academic, 2015.
[10] N. Sharan and S. Mahapatra, "A short-channel common double-gate MOSFET model adapted to gate oxide thickness asymmetry," *IEEE Trans. Electron Devices*, vol. 61, no. 8, pp. 2732–2737, Aug. 2014.
[11] Y. Taur, "An analytical solution to a double-gate MOSFET with undoped body," *IEEE Electron Device Lett.*, vol. 21, no. 5, pp. 245–247, May 2000.
[12] A. Sahoo, P. K. Thakur, and S. Mahapatra, "A computationally efficient generalized poisson solution for independent double-gate transistors," *IEEE Trans. Electron Devices*, vol. 57, no. 3, pp. 632–636, Mar. 2010.
[13] S. Mudanai, A. Roy, R. Kotlyar, T. Rakshit, and M. Stettler, "Capacitance compact model for ultrathin low-electron-effective-mass materials," *IEEE Trans. Electron Devices*, vol. 58, no. 12, pp. 4204–4211, Dec. 2011.
[14] S. Oh and H.-S. P. Wong, "Physics-based compact model of III–V heterostructure FETs for digital logic applications," in *IEDM Tech. Dig.*, Dec. 2008, pp. 1–4.
[15] C. Yadav, J. P. Duarte, S. Khandelwal, A. Agarwal, C. Hu, and Y. S. Chauhan, "Capacitance modeling in III–V FinFETs," *IEEE Trans. Electron Devices*, vol. 62, no. 11, pp. 3892–3897, Nov. 2015.
[16] *Users' Manual of Silvaco ATLAS, Version 5.20.2.R*, accessed on May 2015. [Online]. Available: www.silvaco.com
[17] F. Stern and W. E. Howard, "Properties of semiconductor surface inversion layers in the electric quantum limit," *Phys. Rev.*, vol. 163, no. 3, p. 816, Nov. 1967.
[18] G. Gildenblat, Z. Zhu, and C. C. McAndrew, "Surface potential equation for bulk MOSFET," *Solid State Electron.*, vol. 53, no. 1, pp. 11–13, Jan. 2009.
[19] D. Jimenez, J. J. Saenz, B. Iniguez, J. Sune, L. F. Marsal, and J. Pallares, "Modeling of nanoscale gate-all-around MOSFETs," *IEEE Electron Device Lett.*, vol. 25, no. 5, pp. 314–316, May 2004.
[20] S. L. Chuang, *Physics of Optoelectronic Devices*. Hoboken, NJ, USA: Wiley, 1995.
[21] S. M. Sze, *Physics of Semiconductor Devices*. Hoboken, NJ, USA: Wiley, 1969.

Ananda Sankar Chakraborty received the M.Tech. degree in VLSI design from the Indian Institute of Engineering Science and Technology at Shibpur, Howrah, India, in 2014. He is currently pursuing the Ph.D. degree with the Nano Scale Device Research Laboratory, Department of Electronic Systems Engineering, Indian Institute of Science, Bengaluru, India.

Santanu Mahapatra (M'08–SM'10) received the Ph.D. degree from the École Polytechnique Fédérale de Lausanne, Lausanne, Switzerland, in 2005.

He is currently a Professor with the Indian Institute of Science, Bengaluru, India. His current research interests include atomistic, device and compact modeling.

Dr. Mahapatra was a recipient of the Ramanna Fellowship from the Department of Science and Technology, Government of India, for his contribution in compact modeling, in 2012.